


 Cite this: *RSC Adv.*, 2019, **9**, 31846

Received 5th August 2019
 Accepted 29th September 2019
 DOI: 10.1039/c9ra06066a
rsc.li/rsc-advances

Enhanced capacitive properties of all-metal-oxide-nanoparticle-based asymmetric supercapacitors†

 Sohyun Jin, Haein Lee and Sanggyu Yim *

The major problem of transition metal oxide (TMO)-based supercapacitors is their low specific energy (E_{sp}) due to the poor electrical conductivity of the TMO electrodes and narrow operating voltage window. To solve these limitations simultaneously, we propose asymmetric supercapacitors (ASCs) consisting of two composite TMO electrodes working in different potential ranges. Titanium dioxide (TiO_2) nanoparticle (NP)-incorporated iron oxide (Fe_2O_3) and manganese oxide (MnO_2) NPs were used as electrode materials covering the negative and positive potential window, respectively. The specific capacitance (C_{sp}) of this asymmetric TiO_2 – Fe_2O_3 || TiO_2 – MnO_2 supercapacitor is comparable to that of the symmetric TiO_2 – MnO_2 || TiO_2 – MnO_2 supercapacitor. However, the ASC can operate over a doubly extended voltage range, which resulted in a significant enhancement in the specific energy of the device. The E_{sp} value of the ASC at a specific power of 1000 W kg⁻¹ is 48.6 W h kg⁻¹, which is 34.1 and 8.1 times, respectively, larger than that of the two symmetric devices.

Introduction

Pseudocapacitors have attracted growing attention due to their superior specific capacitance (C_{sp}) compared to other types of supercapacitors, mainly electrical double layer capacitors (EDLCs).^{1–3} The high C_{sp} values of pseudocapacitors are attributed to the faradaic redox reactions of the electrode materials for storing charges while the EDLCs use only non-faradaic charge storage on the electrode surface.^{3,4} Especially, transition metal oxides (TMOs) have been widely investigated as an electrode material for pseudocapacitors due to their high theoretical C_{sp} values and variant redox characteristics.^{5–7}

However, the major limitation of the TMO-based pseudocapacitors is their low energy density due to the intrinsically narrow redox potential of the TMOs because the energy density (E) is proportional to the square of the operating voltage window (ΔV), $E = C_{sp}(\Delta V)^2/2$.^{8,9} To solve this problem, an asymmetric supercapacitor (ASC) has been studied to widen the voltage window by integrating two electrodes with different working potentials. Normally, TMOs with a positive working potential have been used as a positive electrode, while carbon materials such as graphene,^{9,10} activated carbon,^{11,12} and carbon

nanotube¹³ have been used as a negative electrode. However, the relatively low specific capacitance of the carbon-based electrode still hampers the further enhancement of the energy density. Thus, ASCs comprised of two TMO-based electrodes with different redox potentials are a promising candidate. Another challenging fact is that most TMOs have poor electrical conductivity, which leads to a low rate capability and a rapid decrease in the electrode thickness.^{14–16} To overcome this problem, various electrode nanostructures have been proposed to increase the contact between the electrode and electrolyte.^{16–19} Although nanostructured electrodes have improved the capacitive characteristics to some extent, most fabrication techniques are still expensive and complicated for practical use. In contrast, a much simpler, low-cost preparation for a variety of TMO nanoparticles (NPs) has been well established, and hence the TMO NPs are promising materials for nanostructured supercapacitor electrodes. However, very limited studies have been reported on all TMO-NPs-based ASCs; therefore, the preparation and capacitive property of such devices are of significant interest from both a fundamental and technological perspective.

In this study, we developed the ASC consisting of manganese oxide (MnO_2) and iron(III) oxide (Fe_2O_3) NPs-based electrodes. These two TMOs are low-cost, non-toxic and easily obtained from naturally abundant minerals. Furthermore, these TMO-based electrodes work at different potentials, and hence their combination is expected to widen the voltage window of the ASC.^{20–22} The working potentials of the MnO_2 and Fe_2O_3 electrodes were reported as 0.0–1.0 V and –1.1–0.2 V, respectively.^{15,23–26} A small amount of titanium oxide (TiO_2) NPs was also incorporated into the MnO_2 and Fe_2O_3 electrodes for

Department of Chemistry, Kookmin University, Seoul 02707, South Korea. E-mail: sgyim@kookmin.ac.kr; Tel: +82-2-910-4734

† Electronic supplementary information (ESI) available: SEM image of TiO_2 -free Fe_2O_3 and MnO_2 electrodes, TEM images of the TMO electrodes, CVs of TMO electrodes, BET N_2 adsorption–desorption isotherm plots of TMO NPs, FE-SEM images of the electrodes taken before and after the GCD cycle test, summary of deconvolution results of capacitive elements of the TMO-based electrodes, summary of specific capacitances of TMO-based electrodes. See DOI: [10.1039/c9ra06066a](https://doi.org/10.1039/c9ra06066a)



a synergistic improvement of the electrode performance. The incorporation of the TiO_2 NPs was expected to improve the charge transport characteristics of the TMO electrodes because the electrical conductivity of TiO_2 (10^{-5} to 10^{-2} S cm $^{-1}$) is higher than that of MnO_2 (10^{-6} to 10^{-5} S cm $^{-1}$) and Fe_2O_3 (10^{-9} to 10^{-7} S cm $^{-1}$).^{27,28} In addition, the TiO_2 NPs are stable, inexpensive and readily available. The all-TMO-NPs-based ASC with an architecture of $\text{TiO}_2\text{--Fe}_2\text{O}_3\text{||TiO}_2\text{--MnO}_2$ could operate over a significantly extended voltage range of 2.0 V, and hence, its specific energy was approximately 34.1 and 8.1 times larger than those of the $\text{TiO}_2\text{--Fe}_2\text{O}_3\text{||TiO}_2\text{--Fe}_2\text{O}_3$ and $\text{TiO}_2\text{--MnO}_2\text{||TiO}_2\text{--MnO}_2$ symmetric supercapacitors, respectively. Other capacitive properties of the $\text{Fe}_2\text{O}_3\text{||MnO}_2$ -based ASC such as the voltammetric response and cycle life were also investigated.

Experimental

First, the synthetic process for the MnO_2 and Fe_2O_3 NPs from their precursors, potassium permanganate (KMnO_4) and iron(III) nitrate ($\text{Fe}(\text{NO}_3)_3$), respectively, was described elsewhere.²⁹ During the synthesis of the NPs, commercially available TiO_2 NPs (anatase, Dysol) with an average diameter of 10 nm were added to the synthetic reactor for their incorporation. The amount of TiO_2 NPs used was one-tenth the weight of each precursor, which corresponds to 15 wt% for the $\text{TiO}_2\text{--MnO}_2$ composite NPs and 13 wt% for the $\text{TiO}_2\text{--Fe}_2\text{O}_3$ composite NPs, assuming that the reaction proceeded completely. The $\text{TiO}_2\text{--MnO}_2$ electrode was prepared by dipping a nickel foam into a slurry containing $\text{TiO}_2\text{--MnO}_2$ NPs as an active material, super-P as a conductive additive, and polytetrafluoroethylene (PTFE, Aldrich) as a binder with a weight ratio of 8 : 1 : 1. The $\text{TiO}_2\text{--Fe}_2\text{O}_3$ electrode was prepared in a similar manner except that a fluorine-doped tin oxide (FTO) substrate was used instead of Ni foam as a current collector. The loading mass of each electrode was measured using a microbalance. The ASC was prepared by stacking the $\text{TiO}_2\text{--MnO}_2$ electrode and $\text{TiO}_2\text{--Fe}_2\text{O}_3$ electrode with a membrane filter paper as a separator in between.

The morphology and crystalline structure of the synthesized NPs were characterized by field emission scanning electron microscopy (FE-SEM, JSM-7410F, JEOL Ltd.), transmission electron microscopy (TEM, JEM-2100F, JEOL Ltd.), and X-ray diffraction (XRD, Rigaku D/Max2500). The specific surface area of the NPs were also estimated using a Brunauer–Emmett–Teller (BET) surface area analyser (QuadraSorb Station 2, Quantachrome Instrument). The capacitive properties of the electrodes and ASCs were evaluated using a cyclic voltammeter (ZIVE SP2, WonATech) in a 1.0 M aqueous Na_2SO_4 electrolyte solution. While a two electrode system was used for the symmetric and asymmetric full-cell capacitors, a three electrode system, *i.e.* the TMO electrode as a working electrode, a platinum plate as a counter electrode, and Ag/AgCl (in 3 M KCl) as a reference electrode, was used to evaluate the individual electrode.

Results and discussion

The morphologies of the TiO_2 -NPs-embedded Fe_2O_3 and MnO_2 NPs were characterized by FE-SEM (Fig. 1a and b). Uniform,

spherical particles with tens of nanometers in size were clearly observed. The elemental SEM-mapping results for the Ti atoms shown in the inset of the figures indicated that the TiO_2 NPs were well and uniformly dispersed. The Ti/Fe and Ti/Mn atomic ratios determined from the SEM-mapping analyses were equivalent to the mole fraction of TiO_2 used, indicating a stoichiometric embedment of the TiO_2 NPs. The crystallinities of the $\text{TiO}_2\text{--Fe}_2\text{O}_3$ and $\text{TiO}_2\text{--MnO}_2$ composite NPs were characterized by XRD measurements. While clear diffraction patterns corresponding to the hematite $\alpha\text{-Fe}_2\text{O}_3$ phase³⁰ for the $\text{TiO}_2\text{--Fe}_2\text{O}_3$ NPs were observed (Fig. 1c), the broader peaks of the $\text{TiO}_2\text{--MnO}_2$ NPs (Fig. 1d) indicated typical amorphous characteristic of the MnO_2 NPs.^{31–33} Additional diffraction peaks corresponding to the TiO_2 anatase phase were also observed for both composite NPs. More close morphology of the synthesized TMO NPs were observed by TEM (Fig. S2†). In the case of Fe_2O_3 NPs, the clear lattice fringe in the TEM image and spots and rings in the selected area electron diffraction (SAED) pattern indicated the polycrystalline characteristics. In contrast, for the MnO_2 NPs, the fringes and SAED spots were hardly observed, indicating relatively amorphous characteristics, consistent with the XRD results.

Fig. 2a shows the cyclic voltammogram (CV) measured using a three-electrode system at a scan rate of 30 mV s $^{-1}$ for the Fe_2O_3 (negative voltage range) and MnO_2 (positive voltage range) half-cell electrodes with and without TiO_2 incorporation. The specific capacitance, C_{sp} , of the electrodes was calculated by the following equation;

$$C_{\text{sp}} = \frac{I}{m(\text{d}V/\text{dt})} \quad (1)$$

where I (A) is the average current, m (g) is the deposit weight, and $\text{d}V/\text{dt}$ (mV s $^{-1}$) is the scan rate.³⁴ The area of the CV contour, indicative of the specific capacitance, of the $\text{TiO}_2\text{--MnO}_2$ electrode is significantly larger than that of the TiO_2 -free MnO_2 electrode, while the areas of the Fe_2O_3 electrode are little varied.

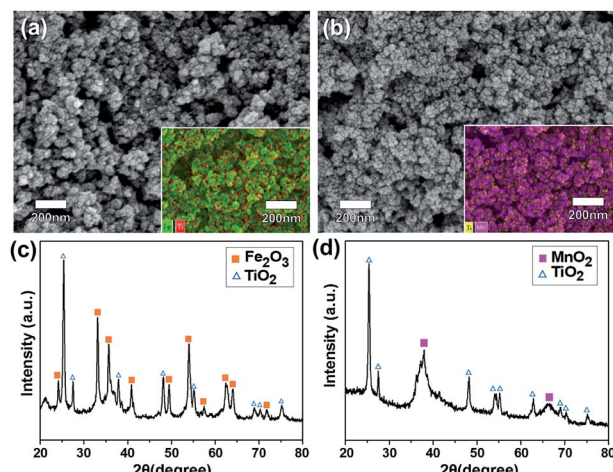


Fig. 1 FE-SEM images of (a) $\text{TiO}_2\text{--Fe}_2\text{O}_3$ and (b) $\text{TiO}_2\text{--MnO}_2$ NPs, and XRD patterns of (c) $\text{TiO}_2\text{--Fe}_2\text{O}_3$ and (d) $\text{TiO}_2\text{--MnO}_2$ NPs. The inset SEM-mapping images for Ti atoms in (a) and (b) show uniform dispersion of the TiO_2 NPs.



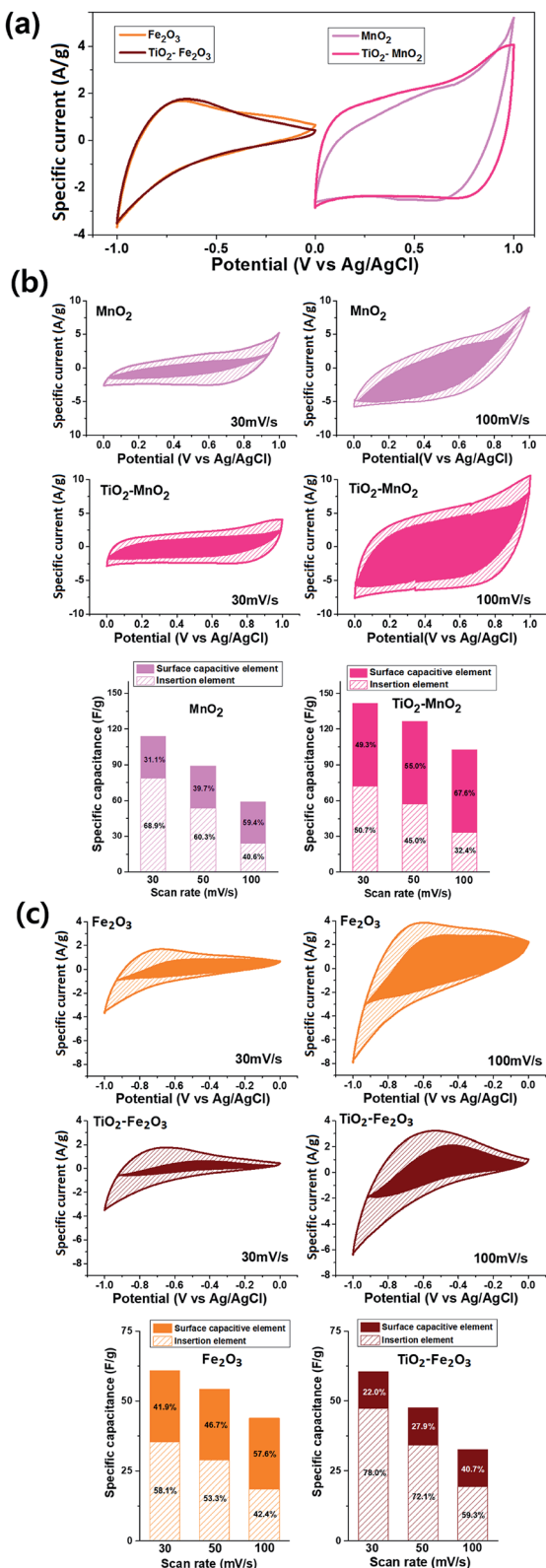


Fig. 2 Cyclic voltammograms of the Fe_2O_3 , $\text{TiO}_2\text{-Fe}_2\text{O}_3$, MnO_2 , $\text{TiO}_2\text{-MnO}_2$ electrodes at a scan rate of 30 mV s^{-1} (a) and deconvolutions of the total capacitance into surface element (solid part) and insertion element (shaded part) for the (b) $\text{TiO}_2\text{-MnO}_2$ and (c) $\text{TiO}_2\text{-Fe}_2\text{O}_3$ electrodes measured at 30 and 100 mV s^{-1} . The bar graphs represent the contribution of each element at various scan rates.

The calculated C_{sp} value of the MnO_2 electrode increased from 114.0 F g^{-1} to 141.5 F g^{-1} after the TiO_2 incorporation. The CVs of the half-cell electrodes before and after TiO_2 incorporation measured at various scan rates are shown in Fig. S3.† More quantitative analyses on the effect of the TiO_2 incorporation were carried out by deconvoluting the capacitive elements of the electrodes. At a given applied voltage, a current is regarded as a sum of the two capacitive elements, namely a surface element ($k_1 v$) and faradaic insertion element ($k_2 v^{1/2}$), according to the following equation;^{35,36}

$$i(V) = k_1 v + k_2 v^{1/2} \quad (2)$$

where v is the scan rate and k_1 , k_2 are constants. The process of extracting elements was described elsewhere.³⁷

The deconvoluted CV graphs for the MnO_2 electrodes at scan rates of 30 mV s^{-1} and 100 mV s^{-1} are shown in Fig. 2b. The $k_1 v$ plot corresponding to the surface capacitive element is shown as a solid area, and the other shaded area corresponds to the insertion element. The surface element of the TiO_2 -free MnO_2 electrode was approximately 34.9 F g^{-1} , which was virtually independent of the scan rate.³⁶ However, the insertion element decreased from 79.0 F g^{-1} at 30 mV s^{-1} to 23.8 F g^{-1} at 100 mV s^{-1} because the diffusion-controlled insertion was less accessible at a higher scan rate.^{38,39} The contribution of the insertion element in the total capacitance hence decreased from 69.3% at 30 mV s^{-1} to 40.5% at 100 mV s^{-1} . The incorporation of the TiO_2 NPs significantly increased the surface element to 69.2 F g^{-1} . The insertion element also increased to 72.3 F g^{-1} at 30 mV s^{-1} and 33.0 F g^{-1} at 100 mV s^{-1} . As a result, at 30 mV s^{-1} , the total specific capacitance of the TiO_2 -incorporated MnO_2 electrode (141.5 F g^{-1}) was 1.24 times larger than that of the TiO_2 -free MnO_2 electrode (114.0 F g^{-1}). At a high scan rate, the effect of the TiO_2 incorporation was more apparent, reaching a 1.73 times increase in C_{sp} from 58.8 F g^{-1} to 102.2 F g^{-1} at 100 mV s^{-1} . This enhancement in specific capacitance and voltammetric response is probably attributed to the reduced resistance of the electrode due to incorporation of electrically more conductive TiO_2 NPs. The resistive elements of the electrodes was evaluated by electrochemical impedance spectroscopy (EIS) measurements (Fig. 3a and b). The diameter of the round curve in the high-frequency region of the Nyquist plots, indicative of the charge-transfer resistance, R_{ct} , were significantly smaller for the TiO_2 -incorporated electrodes. The diffusive resistance, R_{d} , which is inversely proportional to the slope of the line in the low-frequency region, also decreased by the TiO_2 incorporation.

While the incorporation of the TiO_2 NPs improved both the capacitive elements of the MnO_2 -based electrode, only the insertion element was increased in the case of the Fe_2O_3 electrode (Fig. 2c). The scan-rate-independent surface element of the TiO_2 -free Fe_2O_3 electrode was approximately 25.2 F g^{-1} , while the insertion element was 35.6 F g^{-1} (58.1%) at 30 mV s^{-1} and 16.6 F g^{-1} (42.4%) at 100 mV s^{-1} . For the $\text{TiO}_2\text{-Fe}_2\text{O}_3$ electrode, the insertion elements were significantly larger over the whole range of the scan rate, e.g. 47.2 F g^{-1} (78.0%) at 30 mV s^{-1} and 19.3 F g^{-1} (59.3%) at 100 mV s^{-1} , indicating that the incorporation of the TiO_2 NPs improved the diffusion of the



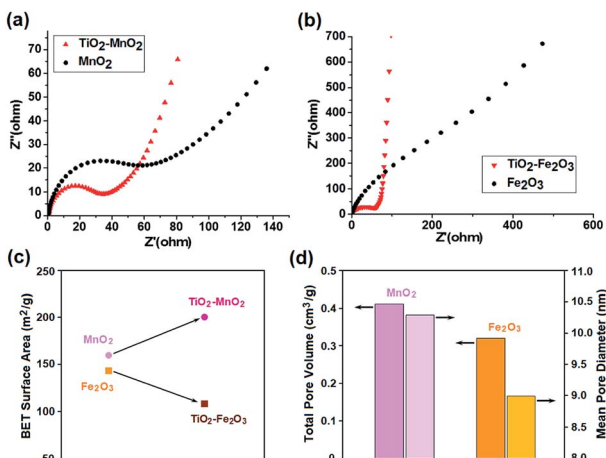


Fig. 3 Nyquist plots of (a) MnO_2 - and (b) Fe_2O_3 -based electrodes, and (c) BET specific surface area and (d) total pore volume and mean pore diameter of the synthesized TMO NPs.

charge carriers in the Fe_2O_3 electrode. In contrast, the TiO_2 incorporation decreased the surface elements from 25.2 F g^{-1} to 13.3 F g^{-1} . The opposite effect of the TiO_2 incorporation on the surface elements of the MnO_2 and Fe_2O_3 electrode is probably related to the change of their surface area. The BET isotherms, with an adsorption-desorption hysteresis loop as shown in Fig. S4,† indicate that the synthesized MnO_2 and Fe_2O_3 NPs can be categorized as a mesoporous adsorbents.⁴⁰ This porous nature of the electrode materials is favourable for the application to supercapacitor electrodes due to the increased surface sites for the energy storage.^{41–44} While the specific surface area of the MnO_2 NPs increased from $137.5 \text{ m}^2 \text{ g}^{-1}$ to $164.3 \text{ m}^2 \text{ g}^{-1}$ by the TiO_2 incorporation, that of the Fe_2O_3 NPs decreased from $142.5 \text{ m}^2 \text{ g}^{-1}$ to $107.5 \text{ m}^2 \text{ g}^{-1}$ (Fig. 3c). Although it is not clear yet, the incorporation of TiO_2 NPs on the MnO_2 NPs with larger pore volume and mean pore diameter (Fig. 3d) might lead to more morphological hierarchization. On the other hand, the TiO_2 incorporation on Fe_2O_3 NPs seemed to result in a reduction of contact sites with the electrolyte. All the deconvolution results are summarized in Tables S1 and S2.†

Based on the results of the two composite TMO NPs-based single electrode cells, an asymmetric full-cell consisting of $\text{TiO}_2\text{-Fe}_2\text{O}_3$ and $\text{TiO}_2\text{-MnO}_2$ electrodes was fabricated. Since the electrochemical redox reactions of the two electrodes occur in entirely different voltage ranges, *i.e.* $-1.0\text{--}0.0 \text{ V}$ for the $\text{TiO}_2\text{-Fe}_2\text{O}_3$ and $0.0\text{--}1.0 \text{ V}$ for the $\text{TiO}_2\text{-MnO}_2$ electrode, the asymmetric combination of the two electrodes was expected to significantly increase the specific energy of the device. The schematic of the ASC device is shown in the inset of Fig. 4c. For comparison, symmetric supercapacitors, *i.e.* devices based on $\text{TiO}_2\text{-Fe}_2\text{O}_3\text{||TiO}_2\text{-Fe}_2\text{O}_3$ and $\text{TiO}_2\text{-MnO}_2\text{||TiO}_2\text{-MnO}_2$ electrodes, were also fabricated. Fig. 4a and b show the CV contours of the $\text{TiO}_2\text{-Fe}_2\text{O}_3$ and $\text{TiO}_2\text{-MnO}_2$ symmetric cell, respectively, at various scan rates from 10 mV s^{-1} to 100 mV s^{-1} . The calculated C_{sp} values are plotted as a function of the scan rate (Fig. 4d). The C_{sp} value of the $\text{TiO}_2\text{-Fe}_2\text{O}_3$ symmetric device was 35.5 F g^{-1} measured at a scan rate of 30 mV s^{-1} . This C_{sp} value is approximately half the value of the $\text{TiO}_2\text{-Fe}_2\text{O}_3$ single electrode,

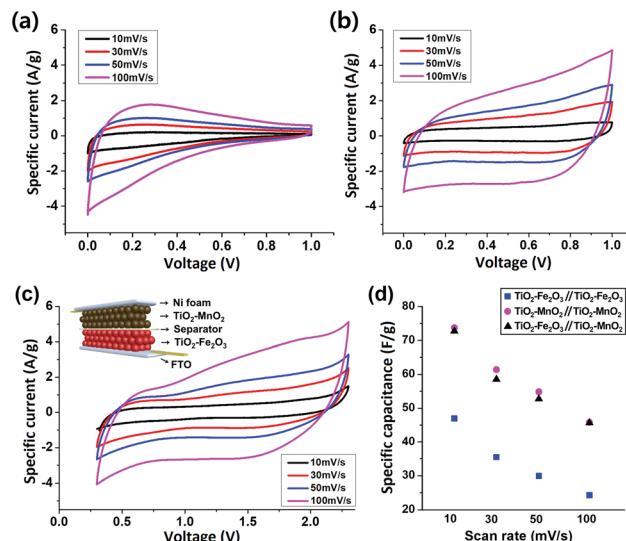


Fig. 4 Cyclic voltammograms of (a) $\text{TiO}_2\text{-Fe}_2\text{O}_3\text{||TiO}_2\text{-Fe}_2\text{O}_3$ symmetric, (b) $\text{TiO}_2\text{-MnO}_2\text{||TiO}_2\text{-MnO}_2$ symmetric and (c) $\text{TiO}_2\text{-Fe}_2\text{O}_3\text{||TiO}_2\text{-MnO}_2$ asymmetric devices at various scan rates. The inset in (c) represents the schematic of the asymmetric device structure. The C_{sp} values of the devices are plotted as a function of the scan rate in (d).

60.5 F g^{-1} , according to the following equation for the C_{sp} calculation of symmetric or asymmetric devices,

$$\frac{1}{C} = \frac{1}{m_+ C_+} + \frac{1}{m_- C_-} \quad (3)$$

where m is the mass, C is the specific capacitance, and $+$ or $-$ denotes the values for positive and negative electrodes, respectively. The C_{sp} value gradually decreased as the scan rate increased, and reached 24.3 F g^{-1} at 100 mV s^{-1} . For the $\text{TiO}_2\text{-MnO}_2$ symmetric device, the C_{sp} decreased from 73.7 F g^{-1} at 10 mV s^{-1} to 45.8 F g^{-1} at 100 mV s^{-1} . The C_{sp} values of the symmetric cells at various scan rates are plotted in Fig. 4d and summarized in Table S3.†

Prior to the assembly of the $\text{TiO}_2\text{-Fe}_2\text{O}_3\text{||TiO}_2\text{-MnO}_2$ ASCs, the mass ratio of the $\text{TiO}_2\text{-Fe}_2\text{O}_3$ and $\text{TiO}_2\text{-MnO}_2$ NPs was determined by the C_{sp} values of the Fe_2O_3 - and MnO_2 -based symmetric cells using the following equation in order to make each electrode contribute equivalent capacitance,

$$R = \frac{m_+}{m_-} = \frac{C_- \Delta V_-}{C_+ \Delta V_+} \quad (4)$$

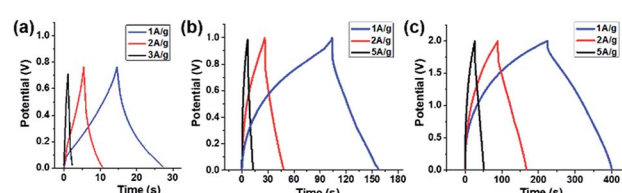


Fig. 5 (a) Galvanostatic charge–discharge curves of (a) $\text{TiO}_2\text{-Fe}_2\text{O}_3\text{||TiO}_2\text{-Fe}_2\text{O}_3$ symmetric, (b) $\text{TiO}_2\text{-MnO}_2\text{||TiO}_2\text{-MnO}_2$ symmetric and (c) $\text{TiO}_2\text{-Fe}_2\text{O}_3\text{||TiO}_2\text{-MnO}_2$ asymmetric devices at various specific currents.



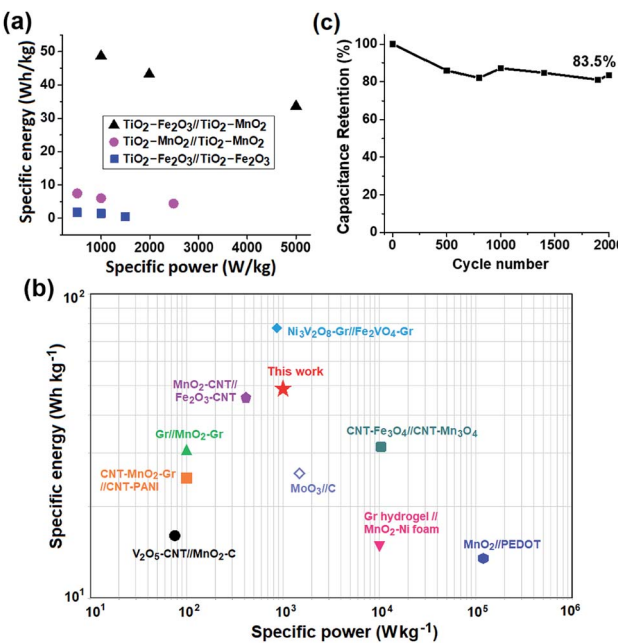


Fig. 6 Ragone plots for (a) Fe₂O₃- and MnO₂-based devices and (b) other ASCs reported in the literature for comparison, and (c) capacitance retention of the TiO₂-Fe₂O₃//TiO₂-MnO₂ ASC as a function of the number of GCD cycles at a specific current of 2 A g⁻¹.

where ΔV_+ and ΔV_- are the voltage windows of the positive and negative electrode, respectively. The measured mass of the TiO₂-Fe₂O₃ and TiO₂-MnO₂ NPs used in this work were 3.5 and 0.8 mg cm⁻², respectively. The CVs of the TiO₂-Fe₂O₃//TiO₂-MnO₂ ASC measured at various scan rates are shown in Fig. 4c, and the calculated C_{sp} values are plotted in Fig. 4d. A working voltage window of 2.0 V was determined by the results of the individual electrode. The C_{sp} values of the ASC were slightly smaller than the values of the TiO₂-MnO₂-based symmetric cell over the entire range of the scan rates. The largest C_{sp} value of 72.7 F g⁻¹ was obtained at a scan rate of 10 mV s⁻¹, and the value decreased to 45.6 F g⁻¹ at 100 mV s⁻¹. This scan rate retention of 62.7% was larger than 51.8% for the TiO₂-Fe₂O₃ symmetric cell and 62.1% for the TiO₂-MnO₂ symmetric cell, as shown in Fig. 4d, indicating a higher voltammetric response of the ASC.

The capacitive performance of the Fe₂O₃- and MnO₂-based symmetric and asymmetric cells were also estimated by galvanostatic charge-discharge (GCD) measurements shown in Fig. 5. The C_{sp} value of the TiO₂-Fe₂O₃ symmetric cell was 12.8, 10.3, and 3.5 F g⁻¹ measured at a current density of 1, 2 and

3 A g⁻¹, respectively (Fig. 5a). The considerably extended discharge time of the TiO₂-MnO₂ symmetric and asymmetric cells (Fig. 5b and c) indicate the better capacitance of the MnO₂-based electrode. The calculated C_{sp} values of the TiO₂-Fe₂O₃//TiO₂-MnO₂ ASC were 87.5, 77.7, and 33.6 F g⁻¹ at a current density of 1, 2 and 5 A g⁻¹, respectively. The obtained C_{sp} values at various current densities are summarized in Table S4.† In addition to the larger C_{sp} value of the TiO₂-Fe₂O₃//TiO₂-MnO₂ ASC, the doubly extended voltage window contributed to the enhancement in the energy density of the device shown in the Ragone plots (Fig. 6a). The specific energy (E_{sp}) and specific power (P_{sp}) of the cells were calculated using the following equations,^{45,46}

$$E_{sp} = \frac{5C_{sp}(\Delta V)^2}{36} \quad (5)$$

$$P_{sp} = \frac{3600E_{sp}}{\Delta t} \quad (6)$$

where ΔV (V) is the applied voltage window and Δt (s) is the discharge time. As shown in the figure, the specific energies of the TiO₂-Fe₂O₃//TiO₂-MnO₂ ASC are larger than those of the symmetric cells at the given specific power. The specific energy of the TiO₂-Fe₂O₃//TiO₂-MnO₂ ASC reached 48.6 W h kg⁻¹ at a specific power of 1000 W kg⁻¹. The E_{sp} values of the all-metal-oxide-NPs-based symmetric and asymmetric supercapacitors are summarized in Table 1. The obtained specific energy of the TiO₂-Fe₂O₃//TiO₂-MnO₂ ASC is comparable to the metal oxide electrode-based ASCs reported in the literature, including CNT-Fe₃O₄//CNT-Mn₃O₄,⁴⁷ graphene (Gr) hydrogel//MnO₂-Ni foam,¹⁰ Gr//MnO₂-Gr,⁴⁸ MnO₂-CNT//Fe₂O₃-CNT,⁴⁹ CNT-MnO₂-Gr//CNT-PANI,⁵⁰ V₂O₅-CNT//MnO₂-C,⁵¹ Ni₃V₂O₈-Gr//Fe₂VO₄-Gr,⁵² MnO₂//PEDOT⁵³ and MoO₃/C⁵⁴ ASCs, as shown in Fig. 6b. The cycle stability of the TiO₂-Fe₂O₃//TiO₂-MnO₂ ASC was also evaluated by repetitive GCD measurement cycles at a specific current of 2 A g⁻¹ (Fig. 6c). The C_{sp} retention after 2000 GCD cycles was 83.5% of the initial value. The apparent change in the surface morphology of the electrodes was not observed after 2000 GCD cycles (Fig. S5†), also indicating the good structural stability of the TiO₂-Fe₂O₃//TiO₂-MnO₂ ASC electrodes.

Conclusions

An all-metal-oxide-NPs-based ASC with electrodes made of TiO₂ NPs-incorporated Fe₂O₃ and MnO₂ NPs was successfully fabricated. In the MnO₂ NPs-based single electrode, the incorporation of the TiO₂ NPs improved the specific capacitance from

Table 1 Summary of the capacitive properties of the TiO₂-Fe₂O₃ and TiO₂-MnO₂ NPs-based symmetric and asymmetric devices

Capacitive properties	TiO ₂ -Fe ₂ O ₃ //TiO ₂ -Fe ₂ O ₃ symmetric	TiO ₂ -MnO ₂ //TiO ₂ -MnO ₂ symmetric	TiO ₂ -Fe ₂ O ₃ //TiO ₂ -MnO ₂ asymmetric
C_{sp} measured at 10 mV s ⁻¹ (F g ⁻¹)	46.9	73.7	72.7
Voltammetric retention	51.8%	62.1%	62.7%
E_{sp} at P_{sp} of 1000 W kg ⁻¹ (W h kg ⁻¹)	1.4	6.0	48.6



114.0 F g⁻¹ to 141.5 F g⁻¹ at a scan rate of 30 mV s⁻¹. The deconvolution of the capacitive elements indicated that this enhancement was attributed to an increase in both the surface element and insertion element. However, for the Fe₂O₃ NPs-based electrode, the insertion element was increased while the surface capacitive element was reduced so that the total capacitance did not improve apparently. An ASC comprised of these two composite TMO electrodes, the TiO₂-Fe₂O₃ and TiO₂-MnO₂ electrodes, was fabricated. The C_{sp} value of the TiO₂-Fe₂O₃||TiO₂-MnO₂ ASC reached 72.7 F g⁻¹ measured at a scan rate of 10 mV s⁻¹, which is slightly lower than the value for the TiO₂-MnO₂||TiO₂-MnO₂ (73.7 F g⁻¹) symmetric capacitors. However, the ASC could operate over a voltage window of 2.0 V, twice as large as that of the symmetric devices, which resulted in a significant enhancement in the specific energy of the device. The specific energy of the TiO₂-Fe₂O₃||TiO₂-MnO₂ ASC was 48.6 W h kg⁻¹ at a specific power of 1000 W kg⁻¹ while that of the TiO₂-Fe₂O₃||TiO₂-Fe₂O₃ and TiO₂-MnO₂||TiO₂-MnO₂ symmetric capacitor was 1.4 and 6.0 W h kg⁻¹, respectively. The C_{sp} retention of the TiO₂-Fe₂O₃||TiO₂-MnO₂ ASC was approximately 83.5% of the initial value after 2000 GCD cycles. All the benefits, *i.e.* wide operating voltage window and comparable specific capacitance, demonstrate that an all-metal-oxide-NPs-based ASC is a promising architecture for high energy density supercapacitors. It also implies that the device performance will be further improved by optimizing the type and composition of the TMO NPs used.

Conflicts of interest

There is no conflicts to declare.

Acknowledgements

This work was supported by National Research Foundation of Korea (NRF) Grant (No. 2016R1A5A1012966 and 2017R1A2B4012375) funded by the Korean Government.

Notes and references

- 1 J. Wang, S. Y. Dong, B. Ding, Y. Wang, X. D. Hao, H. Dou, Y. Y. Xia and X. G. Zhang, *Natl. Sci. Rev.*, 2017, **4**, 71.
- 2 J. Yan, Q. Wang, T. Wei and Z. Fan, *Adv. Energy Mater.*, 2014, **4**, 1300816.
- 3 J. D. Liu and S. B. Lee, *Chem. Commun.*, 2011, **47**, 1384.
- 4 L. L. Zhang and X. S. Zhao, *Chem. Soc. Rev.*, 2009, **38**, 2520.
- 5 K. Zhang, X. Han, Z. Hu, X. Zhang, Z. Tao and J. Chen, *Chem. Soc. Rev.*, 2015, **44**, 699.
- 6 C. Yang, M. Sun and H. Lu, *Chem.-Eur. J.*, 2018, **24**, 6169.
- 7 P. Sennu, V. Aravindan and Y. S. Lee, *J. Power Sources*, 2016, **306**, 248.
- 8 L. Demarconnay, E. Raymundo-Piñero and F. Béguin, *J. Power Sources*, 2011, **196**, 580.
- 9 J. Yan, Z. Fan, W. Sun, G. Ning, T. Wei, Q. Zhang, R. Zhang, L. Zhi and F. Wei, *Adv. Funct. Mater.*, 2012, **22**, 2632.
- 10 H. Gao, F. Xiao, C. B. Ching and H. Duan, *ACS Appl. Mater. Interfaces*, 2012, **4**, 2801.

- 11 T. Cottineau, M. Toupin, T. Delahaye, T. Brousse and D. Bélandger, *Appl. Phys. A*, 2006, **82**, 599.
- 12 S. T. Senthilkumar, R. K. Selvan, M. Ulaganathan and J. S. Melo, *Electrochim. Acta*, 2014, **115**, 518.
- 13 S. W. Zhang, B. S. Yin, c. Liu, Z. B. Wang and D. M. Gu, *Appl. Surf. Sci.*, 2018, **458**, 478.
- 14 M. Toupin, T. Brousse and D. Bélanger, *Chem. Mater.*, 2004, **16**, 3184.
- 15 I. Ryu, G. Kim, H. Yoon, S. J. Ahn and S. Yim, *RSC Adv.*, 2016, **6**, 102814.
- 16 G. Kim, I. Ryu and S. Yim, *Sci. Rep.*, 2017, **7**, 8260.
- 17 R. S. Kate, S. A. Khalate and R. J. Deokate, *J. Alloys Compd.*, 2018, **734**, 89.
- 18 Z. Yu, L. Tetard, L. Zhai and J. Thomas, *Energy Environ. Sci.*, 2015, **8**, 702.
- 19 D. Hong and S. Yim, *RuO₂*, *Langmuir*, 2018, **34**, 4249.
- 20 Y. Liu, D. Luo, K. Shi, X. Michaud and I. Zhitomirsky, *Nano-Struct. Nano-Objects*, 2018, **15**, 98.
- 21 G. S. Gund, D. P. Dubal, N. R. Chodankar, J. Y. Cho, P. Gomez-Romero, C. Park and C. D. Lokhande, *Sci. Rep.*, 2015, **5**, 12454.
- 22 Z. Liu, X. Tian, X. Xu, L. He, M. Yan, C. Han, Y. Li, W. Yang and L. Mai, *Nano Res.*, 2017, **10**, 2471.
- 23 S. C. Pang, M. A. Anderson and T. W. Chapman, *J. Electrochem. Soc.*, 2000, **147**, 444.
- 24 Y. Hu, C. Guan, Q. Ke, Z. F. Yow, C. Cheng and J. Wang, *Chem. Mater.*, 2016, **28**, 7296.
- 25 A. A. Yadav, *J. Mater. Sci.: Mater. Electron.*, 2016, **27**, 12876.
- 26 P. Y. Tang, L. J. Han, A. Genc, Y. M. He, X. Zhang, L. Zhang, J. R. Galán-Mascarós, J. R. Morante and J. Arbiol, *Nano Energy*, 2016, **22**, 189.
- 27 S. Ito, Y. Yui and J. Mizuguchi, *Mater. Trans.*, 2010, **51**, 1163.
- 28 X. Lu, M. Yu, G. Wang, T. Zhai, S. Xie, Y. Ling, Y. Tong and Y. Li, *Adv. Mater.*, 2013, **25**, 267.
- 29 G. Kim, J. Kang, G. Choe and S. Yim, *Int. J. Electrochem. Sci.*, 2017, **12**, 10015.
- 30 A. Lassoued, B. Dkhil, A. Gadri and S. Ammar, *Results Phys.*, 2017, **7**, 3007.
- 31 S. Li, L. Qi, L. Lu and H. Wang, *RSC Adv.*, 2012, **2**, 3298.
- 32 H. Xingkang, L. Dongping, Y. Hongjun, A. Adel and Y. Yong, *Nanotechnology*, 2008, **19**, 225606.
- 33 A. Zolfaghari, F. Ataherian, M. Ghaemi and A. Gholami, *Electrochim. Acta*, 2007, **52**, 2806.
- 34 C. D. Lokhande, D. P. Dubal and O.-S. Joo, *Curr. Appl. Phys.*, 2011, **11**, 255.
- 35 T.-C. Liu, W. G. Pell, B. E. Conway and S. L. Roberson, *J. Electrochem. Soc.*, 1998, **145**, 1882.
- 36 J. Wang, J. Polleux, J. Lim and B. Dunn, *J. Phys. Chem. C*, 2007, **111**, 14925.
- 37 I. Ryu, G. Kim, D. Park and S. Yim, *J. Power Sources*, 2015, **297**, 98.
- 38 W. Yan, T. Ayvazian, J. Kim, Y. Liu, K. C. Donavan, W. Xing, Y. Yang, J. C. Hemminger and R. M. Penner, *ACS Nano*, 2011, **5**, 8275.
- 39 J. Duay, S. A. Sherrill, Z. Gui, E. Gillette and S. B. Lee, *ACS Nano*, 2013, **7**, 1200.



40 K. S. W. Sing, D. H. Everett, R. A. W. Haul, L. Moscou, R. A. Pierotti, J. Rouquerol and T. Siemieniewska, *Pure Appl. Chem.*, 1985, **570**, 603.

41 J. Cherusseri, K. S. Kumar, N. Choudhary, N. Nagaiah, Y. Jung, T. Roy and J. Thomas, *Nanotechnology*, 2019, **30**, 202001.

42 D. Wang, Y. Xiao, X. Luo, Z. Wu, Y.-J. Wang and B. Fang, *ACS Sustainable Chem. Eng.*, 2017, **5**, 2509.

43 Y.-Z. Wei, B. Fang, S. Iwasa and M. Kumagai, *J. Power Sources*, 2005, **141**, 386.

44 B. Fang, J. H. Kim, M.-S. Kim, A. Bonakdarpour, A. Lam, D. P. Wilkinson and J.-S. Yu, *J. Mater. Chem.*, 2012, **22**, 19031.

45 V. Khomenko, E. Raymundo-Piñero and F. Béguin, *J. Power Sources*, 2006, **153**, 183.

46 T. Brousse, P.-L. Taberna, O. Crosnier, R. Dugas, P. Guilletet, Y. Scudeller, Y. Zhou, F. Favier, D. Bélanger and P. Simon, *J. Power Sources*, 2007, **173**, 633.

47 A. Kumar, D. Sarkar, S. Mukherjee, S. Patil, D. D. Sarma and A. Shukla, *ACS Appl. Mater. Interfaces*, 2018, **10**, 42484.

48 Z.-S. Wu, W. Ren, D.-W. Wang, F. Li, B. Liu and H.-M. Cheng, *ACS Nano*, 2010, **4**, 5835.

49 T. Gu and B. Wei, *J. Mater. Chem. A*, 2016, **4**, 12289.

50 Y. Jin, H. Chen, M. Chen, N. Liu and Q. Li, *ACS Appl. Mater. Interfaces*, 2013, **5**, 3408.

51 Z. Chen, Y. Qin, D. Weng, Q. Xiao, Y. Peng, X. Wang, H. Li, F. Wei and Y. Lu, *Adv. Funct. Mater.*, 2009, **19**, 3420.

52 M. Guo, J. Balamurugan, N. H. Kim and J. H. Lee, *Appl. Catal., B*, 2018, **239**, 290.

53 V. Khomenko, E. Raymundo-Piñero, E. Frackowiak and F. Beguin, *Appl. Phys. A*, 2006, **82**, 567.

54 L. Wang, L. Gao, J. Wang and Y. Shen, *J. Mater. Sci.*, 2019, **54**, 13685.

